Pergamon

Int. J. Heat Mass Transfer. Vol. 41, No. 1, pp. 89–99, 1998

Printed in Great Britain
0017–9310/98 $19.00+0.00

PII: S0017–9310(97)00092–6

Numerical simulation of melting of a horizontal substrate placed beneath a heavier liquid

G. SON and V. K. DHIR

Mechanical and Aerospace Engineering Department, University of California, Los Angeles, Los Angeles, CA 90095, U.S.A.

(*Received* 26 *September* 1996 *and in final form* 21 *March* 1997)

Abstract—In this work, the melting of a horizontal substrate placed beneath a heavier liquid is simulated numerically. A finite difference method is used to solve simultaneously the equations governing the conservation of mass, momentum and energy in the liquid–liquid layers. The equations for the two phases are coupled through the matching of normal and tangential stresses and continuity of mass at the interface. A second-order projection method is employed for decoupling velocities from pressure. A numerical grid generation method is used to construct a grid system, which is aligned with the interface. The numerical results are compared with experimental data reported in the literature. © 1997 Elsevier Science Ltd.

INTRODUCTION

The behavior of the interface between horizontal layers of a heavier liquid overlying a lighter fluid is governed by Taylor instability. The concept of this instability has been applied in the past to analyze a variety of physical phenomena, such as film boiling, maximum and minimum pool boiling heat fluxes, condensation on the underside of a surface and melting or sublimation of a substrate placed beneath a pool of heavier liquid.

Zuber [1] was the first to apply the concept of Taylor instability to predict maximum and minimum heat fluxes for pool boiling. He proposed that vapor bubbles were spaced a distance bounded between the two-dimensional 'critical' and 'most dangerous' Taylor wavelengths. Considering that two bubbles were released per cycle from a square cell, he predicted the minimum heat flux.

Subsequently, Berenson [2] obtained an expression for the heat transfer coefficient during saturated film boiling on horizontal surfaces. Berenson assumed that vapor bubbles were placed on a square grid with a spacing equal to the two-dimensional 'most dangerous' Taylor wavelength, λ_{d2}, and a thin vapor film of uniform thickness connected the neighboring bubbles. By further assuming that mean bubble height and bubble diameter were proportional to the bubble spacing, and two bubbles were supported per λ_{d2}^2 area of the heater, he predicted the film boiling Nusselt number based on average heat transfer coefficient as

$$Nu = 0.42\left[\frac{\rho_v(\rho_l-\rho_v)gh_{fg}}{k_v\mu_v\Delta T}\right]^{1/4}\left[\frac{\gamma}{g(\rho_l-\rho_v)}\right]^{3/8}. \quad (1)$$

In equation (1) all of the properties were evaluated at the mean film temperature. Equation (1) was derived from a static model which did not account for the time variation of the bubble height or bubble diameter and the flow field in the liquid. Heater surface temperature was assumed to remain constant with time and space. In reality the interface is dynamic and temperature and local heat flux can vary during the evolution of the interface. The predictions from equation (1) were, however, found to compare well with Berenson's data. The two-dimensional (2-D) wave configuration used by Zuber and Berenson was improved by Sernas *et al.* [3] while carrying out three-dimensional (3-D) Taylor instability analysis. They showed that using the 3-D Taylor wavelength, λ_{d3}, which is $\sqrt{2}$ times larger than the 2-D Taylor wavelength, four bubbles were released per cycle on λ_{d3}^2 area. Therefore, two bubbles are indeed generated per cycle on λ_{d2}^2 area. However, at any instant there is only one bubble per λ_{d2}^2 that is growing.

Dhir *et al.* [4] studied pseudo film boiling during sublimation of a slab of dry ice placed beneath a pool of warm liquid. The heat transfer rate was determined by noting a change in the enthalpy of the overlying liquid pool. Data were found to compare favorably with the prediction from an equation similar to equation (1) when the lead constant was reduced to 0.36. It was argued that a reduction of about 15% in the lead constant resulted from the fact that during sublimation only one bubble was supported per λ_{d2}^2 area instead of $\lambda_{d2}^2/2$ as assumed by Berenson. This was based on their experimental observation that the bubbles were released from the same location rather than alternately from nodes and antinodes as observed during film boiling on flat plates or during early period of sublimation. Subsequently Taghavi-Tafreshi *et al.* [5] studied melting of a slab of frozen olive oil placed under a pool of water and again found their data to correlate well with predictions from an equation

NOMENCLATURE

C differential operator with convection terms
c_p specific heat at constant pressure
g gravitational acceleration
h heat transfer coefficient
h_{fg} latent heat of evaporation
h_{fs} latent heat of fusion
J Jacobian of transformation, $x_\xi y_\eta - x_\eta y_\xi$
k thermal conductivity
L differential operator with diffusion terms
l_0 characteristic length, $\sqrt{\gamma/g(\rho_2-\rho_1)}$
M, N differential operator with pressure terms
$\underline{Nu}$ Nusselt number, hl_0/k
$\overline{Nu}$ Nusselt number averaged over a cell area
$\overline{\overline{Nu}}$ Nusselt number averaged over a cell area and time
P, Q control functions for grid generation
p dimensionless pressure
p' pressure correction
Pr Prandlt number for fluid 1, $c_{p1}\mu_1/k_1$
R dimensionless radius
r, y dimensionless cylindrical coordinate
Re_i Reynolds number, $\rho_i u_0 l_0/\mu_i$
S source term
T temperature
ΔT temperature difference, $T_{int}-T_{solid}$
t dimensionless time
t_0 characteristic time, $\sqrt{l_0/g}$
u, v dimensionless velocities in r- and y-directions
$\bar{u}, \bar{v}$ dimensionless contravariant velocity components
u_0 characteristic velocity, $\sqrt{gl_0}$
v_0 dimensionless blowing velocity.

Greek symbols

γ surface tension
δ dimensionless film thickness
δ_0 dimensionless undisturbed film thickness
η, ξ transformed coordinates
θ dimensionless temperature
κ dimensionless interfacial curvature
λ_{d2} two-dimensional 'most dangerous' wavelength
λ_{d3} three-dimensional 'most dangerous' wavelength
μ viscosity
ρ density
σ dimensionless viscous normal stress
τ dimensionless shear stress
ϕ general dependent variable
ω growth rate corresponding to λ_{d2}.

Superscripts

n time step of $n\Delta t$
$\hat{}$ property ratio of fluid 1 to fluid 2.

Subscripts

i 1, 2 for fluid 1 and fluid 2
int fluid–fluid interface
l, v liquid, vapor
r, y partial differentiation with respect to r, y
solid solid surface
t partial differentiation with respect to t
ξ, η partial differentiation with respect to ξ, η.

similar to equation (1). However, the lead constant had to be reduced by almost a factor of 2. The reduction in the lead constant was rationalized on the basis that growth rate of the melt droplets was very slow and the time averaged height of the droplets was much smaller than that of a bubble in film boiling. This reduction in lead constant suggests that density difference between the phases or components is an independent parameter in addition to the thermophysical properties already contained in the expression given by equation (1).

Taghavi-Tafreshi and Dhir [6] performed generalized linear Taylor stability analysis that included surface tension, viscosity and layer thickness. They applied the linear analysis to a variety of two-phase processes and compared the 'most dangerous' wavelengths predicted theoretically with the available experimental data. It was found that during film boiling the thickness of vapor layer did not affect the 'most dangerous' wavelength, whereas during melting, certain combinations of liquid layer viscosity and thickness could reduce the 'most dangerous' wavelength predicted from inviscid infinite layer analyses. They also noted that the observed growth rate of the interface was lower than that predicted from the linear Taylor instability theory. However, in the absence of a quantitative basis for the determination of the average film thickness they did not provide an explanation for the difference.

The correlation of Berenson is useful for engineering applications. However, the correlation contributes little to our understanding of the process. As such the purpose of this work is to solve numerically conservation equations of mass, momentum and energy for the liquid–liquid phases during melting process. These equations when solved with appro-

priate interfacial and boundary conditions will also provide a numerical simulation of the evolution of the interface with time. The results of the analysis will yield the rate of heat transfer in the film and droplet regions as well as help delineate the validity of the assumptions made in the various analyses.

ANALYSIS

Figure 1 shows the configuration used in this study to simulate the instability of a horizontal liquid layer between the surface of a melting solid and a large finite layer of warm liquid above. The computation is restricted to 2-D incompressible, and laminar flow which is described in axisymmetric radial coordinates. This axisymmetrical approximation may not be so restrictive and has been verified from the experimental observation of the liquid bulges associated with melting [5] and of vapor bubbles during film boiling [2]. It is further assumed that the solid and the interface are maintained at their specified temperature.

In carrying out numerical simulation characteristic length, l_0, characteristic time, t_0 and characteristic velocity, u_0, are defined as

$$l_0 = \sqrt{\frac{\gamma}{g(\rho_2 - \rho_1)}}; \quad t_0 = \sqrt{\frac{l_0}{g}}, \quad u_0 = \frac{l_0}{t_0}. \tag{2}$$

Also, vapor and liquid pressures are non-dimensionalized with $\rho_v u_0^2$ and $\rho_l u_0^2$ respectively and dimensionless temperature is defined as

$$\theta = \frac{T - T_{\text{solid}}}{T_{\text{int}} - T_{\text{solid}}}. \tag{3}$$

In dimensionless form the equations governing the conservation of mass, momentum, and energy for liquid 1 and liquid 2 are written as

$$(ru_i)_r + (rv_i)_y = 0 \tag{4}$$

$$\frac{Du_i}{Dt} = -p_{ir} + \frac{1}{Re_i}\left(\nabla^2 u_i - \frac{u_i}{r^2}\right) \tag{5}$$

$$\frac{Dv_i}{Dt} = -p_{iy} + \frac{1}{Re_i}\nabla^2 v_i \quad (i = 1, 2) \tag{6}$$

$$\frac{D\theta}{Dt} = \frac{1}{PrRe_1}\nabla^2\theta \tag{7}$$

where p is a pressure modified to remove the body force term in the momentum equation and for general dependent variable, ϕ, which represents dependent variables, u, v, p and θ, the total derivative and the Laplacian can be written as

$$\frac{D\phi}{Dt} = \phi_t + u\phi_r + v\phi_y \tag{8}$$

$$\nabla^2\phi = \frac{1}{r}(r\phi_r)_r + \phi_{yy} \tag{9}$$

also

$$Re_i = \frac{\rho_i u_0 l_0}{\mu_i}; \quad Pr = \frac{c_{pl}\mu_1}{k_1}.$$

Since two-phase flow with a complex interface is difficult to solve in (r, y) coordinates, the following coordinate transformation is used:

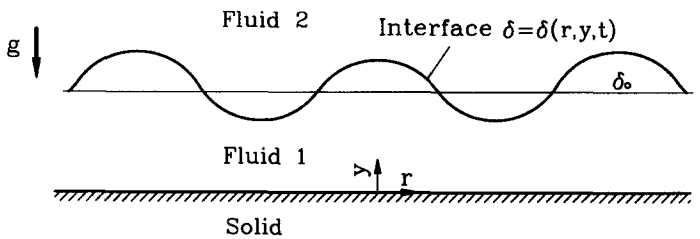

(a)

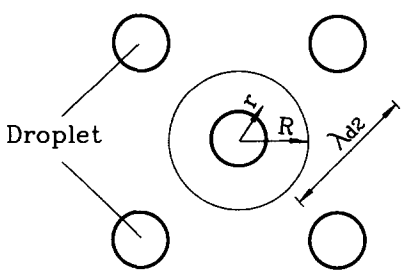

(b)

Fig. 1. Configuration of two layers for melting: (a) side view; and (b) top view for one cell.

$$\xi = \xi(r, y, t); \quad \eta = \eta(r, y, t) \tag{10}$$

where the interface is described by $\eta =$ constant. Using the chain rule of partial differentiation, the governing equations are transformed as:

$$(ry_\eta - rr_\eta v)_\xi + (rr_\xi v - ry_\xi u)_\eta = 0 \tag{11}$$

$$rJu_t + rJp_r = L(u) - C(u) + S_u \tag{12}$$

$$rJv_t + rJp_y = L(v) - C(v) \tag{13}$$

$$rJ\theta_t = Pr^{-1}L(\theta) - C(\theta) \tag{14}$$

where

$$J = r_\xi y_\eta - r_\eta y_\xi$$

$$L(\phi) = Re_i^{-1} J \nabla^2 \phi$$

$$C(\phi) = [ry_\eta(u - r_t) - rr_\eta(v - y_t)]\phi_\xi + [rr_\xi(v - y_t) - ry_\xi(u - r_t)]\phi_\eta$$

$$S_u = -(Re_i r)^{-1} Ju.$$

In this study, a staggered grid system is used in which the locations for velocity components are displaced from those for pressure and temperature. This is done to avoid the difficulty caused by pressure boundary conditions. Also, contravariant velocity components which are naturally dependent variables describing the continuity equation are used as dependent variables. They are defined in this study as

$$\bar{u} = \frac{y_\eta u - r_\eta v}{\sqrt{r_\eta^2 + y_\eta^2}}; \quad \bar{v} = \frac{-y_\xi u + r_\xi v}{\sqrt{r_\xi^2 + y_\xi^2}}. \tag{15}$$

The governing equations for contravariant velocity components are obtained by following the procedure similar to that used by Karki and Patankar [7]. First, the differential equations for cylindrical velocity components which are supposed to be located at the same grid points with contravariant velocity components are discretized spatially using central difference scheme. Thereafter, the discretized governing equations for contravariant velocity components are obtained by algebraic manipulation. When discretizing governing equations temporally, the diffusion terms are treated by fully implicit scheme and the convection, grid curvature and source terms by first-order explicit method. The discretized governing equations are expressed as

$$rJ\frac{\bar{u}^{n+1}}{\Delta t} = -rJM(p^{n+1}) + L(\bar{u}^{n-1}) + S_{\bar{u}}^n \tag{16}$$

$$rJ\frac{\bar{v}^{n+1}}{\Delta t} = -rJN(p^{n+1}) + L(\bar{v}^{n+1}) + S_{\bar{v}}^n \tag{17}$$

where

$$M(p) = \frac{1}{\sqrt{r_\eta^2 + y_\eta^2}}\left(\frac{r_\eta^2 + y_\eta^2}{J}p_\xi - \frac{r_\xi r_\eta + y_\xi y_\eta}{J}p_\eta\right)$$

$$N(p) = \frac{1}{\sqrt{r_\xi^2 + y_\xi^2}}\left(-\frac{r_\xi r_\eta + y_\xi y_\xi}{J}p_\xi + \frac{r_\xi^2 + y_\xi^2}{J}p_\eta\right)$$

$$S_{\bar{u}} = -L(\bar{u}) - \frac{r_\eta}{\sqrt{r_\eta^2 + y_\eta^2}}\left[L(v) + rJ\frac{v}{\Delta t} - C(v)\right] + \frac{y_\eta}{\sqrt{r_\eta^2 + y_\eta^2}}\left[L(u) + rJ\frac{u}{\Delta t} - C(u) + S_u\right]$$

$$S_{\bar{v}} = -L(\bar{v}) + \frac{r_\xi}{\sqrt{r_\xi^2 + y_\xi^2}}\left[L(v) + rJ\frac{v}{\Delta t} - C(v)\right] - \frac{y_\xi}{\sqrt{r_\xi^2 + y_\xi^2}}\left[L(u) + rJ\frac{u}{\Delta t} - C(u) + S_u\right]$$

where superscript ^{n} and $^{n+1}$ represent n and $n+1$ time steps respectively and geometric functions are evaluated at the current time step. In order to obtain governing equation for pressure which achieves mass conservation, the fractional-step method, or projection method, is used. This method has been developed by Chorin [8], Kim and Moin [9], Bell *et al.* [10], Rosenfeld *et al.* [11] and Jin and Braza [12]. Using contravariant velocities as dependent variables, Rosenfeld *et al.* applied the fractional-step method to generalized coordinate systems. A variation of that method is used in the present study.

$$rJ\frac{\theta^{n+1} - \theta^n}{\Delta t} = Pr^{-1}L(\theta^{n+1}) + S_\theta^n \tag{18}$$

$$rJ\frac{\bar{u}^*}{\Delta t} = -rJM(p^n) + L(\bar{u}^*) + S_{\bar{u}}^n \tag{19}$$

$$rJ\frac{\bar{v}^*}{\Delta t} = -rJN(p^n) + L(\bar{v}^*) + S_{\bar{v}}^n \tag{20}$$

$$\bar{u}^{n+1} = \bar{u}^* - \Delta t M(p') \tag{21}$$

$$\bar{v}^{n+1} = \bar{v}^* - \Delta t N(p'). \tag{22}$$

The momentum equations are decomposed into two fractional steps. First the momentum equations (19) and (20) are solved using pressure evaluated at the previous time step. Then, the resulting velocities, $\bar{u}^*$ and $\bar{v}^*$, which do not satisfy the continuity equation, are corrected as given by equations (21) and (22). A pressure correction, p', is estimated as:

$$p^{n+1} = p^n + p' + O(p'\Delta t). \tag{23}$$

Using equations (21), (22) and continuity equation (11), the governing equation for pressure correction is obtained as

$$rJ\nabla^2 p' = \frac{1}{\Delta t}[(\gamma\sqrt{\gamma_\eta^2 + y_\eta^2}\bar{u}^*)_\xi + (\gamma\sqrt{\gamma_\xi^2 + y_\xi^2}\bar{v}^*)_\eta]. \tag{24}$$

At the interface, the matching conditions for velocities and stresses are

$$u_2 - u_1 = 0$$

$$v_2 - v_1 = 0$$

$$\frac{1}{\hat{\mu}}\tau_2 - \tau_1 = 0$$

$$\frac{1}{\hat{\rho}}p_2 - p_1 = \frac{1}{Re_1}\left(\frac{1}{\hat{\mu}}\sigma_2 - \sigma_1\right) + \frac{(1-\hat{\rho})}{\hat{\rho}}(y-\kappa). \quad (25)$$

In the above equations

$$\hat{\rho} = \frac{\rho_1}{\rho_2}; \quad \hat{\mu} = \frac{\mu_1}{\mu_2}$$

$$\tau = \frac{r_\xi^2 + y_\xi^2}{J}\frac{r_\xi u_\eta + y_\xi v_\eta}{r_\xi^2 + y_\xi^2} + \frac{r_\xi v_\xi - y_\xi u_\xi}{r_\xi^2 + y_\xi^2}$$

$$- \frac{r_\xi r_\eta + y_\xi y_\eta}{J}\frac{r_\xi u_\xi + y_\xi v_\xi}{r_\xi^2 + y_\xi^2}$$

$$\sigma = -\frac{2u}{r} - \frac{2(r_\xi u_\xi + y_\xi v_\xi)}{r_\xi^2 + y_\xi^2}$$

$$\kappa = -\frac{r_\xi y_{\xi\xi} - y_\xi r_{\xi\xi}}{(r_\xi^2 + y_\xi^2)^{3/2}} - \frac{y_\xi}{r\sqrt{r_\xi^2 + y_\xi^2}}. \quad (26)$$

Since it is assumed that the interface is maintained at its specified temperature,

$$\theta = 1. \quad (27)$$

At the solid surface

$$u = 0$$

$$v = v_0 = \frac{c_{p1}\Delta T}{h_{fs} Pr_1 Re_1}\theta_y$$

$$\theta = 0. \quad (28)$$

Considering the blowing velocity, v_0, the melting surface is treated as stationary instead of moving. This replacement gives little difference to the liquid–liquid interface behavior because the melting rate of the solid surface is much smaller than the growth rate of the liquid–liquid interface. At the locations of symmetry with respect to y-axis and the centerline,

$$u = v_r = \theta_r = 0. \quad (29)$$

Far away from the interface,

$$u_y = v_y = 0. \quad (30)$$

After solving for the temperature and flow field, the interface is advanced in an explicit manner:

$$r^{n+1} = r^n + \Delta t r_t^n \quad (31)$$

$$y^{n+1} = y^n + \Delta t y_t^n \quad (32)$$

where r_t and y_t are r- and y-directional components of the normal interfacial velocity and are expressed as:

$$r_t = -\frac{y_\xi \bar{v}_1}{\sqrt{(r_\xi^2 + y_\xi^2)}}; \quad y_t = \frac{r_\xi \bar{v}_1}{\sqrt{(r_\xi^2 + y_\xi^2)}}. \quad (33)$$

When the interface is deformed significantly, the interior grid points are difficult to determine algebraically. As such a grid system aligned with a complex interface is generated numerically by solving Poisson's equations [13]. The grid generation equation is

$$\nabla^2 \xi = P(\xi_r^2 + \xi_y^2); \quad \nabla^2 \eta = Q(\eta_r^2 + \eta_y^2) \quad (34)$$

where P and Q are functions which control the spacing and curvatures of η and ξ grid lines. Without the control functions, the interior grid points would be uniformly spaced away from the boundary regardless of the boundary grid point distribution because of the strong smoothing tendencies of Laplace equations. The control functions, P and Q, are evaluated in the same manner as was done by Thompson [14] and Thompson *et al.* [13]. They are expressed as:

$$P = -\frac{r_\xi r_{\xi\xi} + y_\xi y_{\xi\xi}}{r_\xi^2 + y_\xi^2} - \sqrt{r_\xi^2 + y_\xi^2}\frac{y_\eta r_{\eta\eta} - r_\eta y_{\eta\eta}}{(r_\eta^2 + y_\eta^2)^{1.5}} \quad (35)$$

$$Q = -\frac{r_\eta r_{\eta\eta} + y_\eta y_{\eta\eta}}{r_\eta^2 + y_\eta^2} - \sqrt{r_\eta^2 + y_\eta^2}\frac{r_\xi y_{\xi\xi} - y_\xi r_{\xi\xi}}{(r_\xi^2 + y_\xi^2)^{1.5}}. \quad (36)$$

The first and second terms of equations (35) and (36) control the spacing and curvatures of grid lines, respectively. These functions are evaluated at the boundary first and are then interpolated linearly into the computational domain.

In this study, the discretized equations are solved iteratively by a line-by-line tridiagonal-matrix algorithm supplemented by Gauss–Seidal method which was suggested by Patankar [15]. To enhance the rate of iteration convergence, a relaxation factor obtained from orthogonal-residual method [16] is used. During computations, the optimal relaxation factor enhanced the rate of iteration convergence significantly compared with the initially specified and fixed relaxation factor.

RESULTS AND DISCUSSION

The instability of the horizontal liquid layer between the surface of a melting solid and a large finite layer of warm liquid supported above the substrate was simulated. Symmetry was assumed to exist at $r = 0$ and at $r = R = \lambda_{d2}/\sqrt{\pi}$. The latter condition corresponds to the assumption that one liquid droplet is released per λ_{d2}^2 area of the melting surface per cycle [Fig. 1(b)]. In order to be able to compare the numerical results with the data of Taghavi-Tafreshi *et al.* [5], the solid was taken to be frozen olive oil, and the overlying liquid layer to be water. The 'most dangerous' wavelength, λ_{d2}, can be obtained from generalized linear stability analysis that include surface tension, viscosity and layer thickness. During numerical simulation, λ_{d2} is set equal to 9.33, which is corresponding to the 'most dangerous' wavelength for $\delta_0 = 0.5$. This

Table 1. Dependence of λ_{d2} and ω on the melt layer thickness predicted from the linear stability analysis

δ_0	λ_{d2}	ω
1.00	10.1	3.59×10^{-2}
0.50	9.33	7.66×10^{-3}
0.40	9.18	4.22×10^{-3}
0.35	9.12	2.92×10^{-3}
0.30	9.06	1.89×10^{-3}
0.10	8.91	7.53×10^{-5}

approximation is deemed reasonable for a thin melt layer ($\delta_0 \leqslant 1$) because the variation of the 'most dangerous' wavelength with δ_0 is small as shown in Table 1.

Figure 2 shows the evolution of the liquid–liquid interface for $T_{int} - T_{solid}$ of 17.5°C. Here, the peak is at $r = 0$ and the valley is at $r = R$. A comparison of the evolution of the peak and valley regions indicates that the growth of the interface in the peak region is much more pronounced than the downward movement of the interface in the valley region where the interface movement is retarded by the presence of the melting surface. After the peak attains an amplitude of about two, its growth rate accelerates with time. It is caused by the squeezing effect which results mainly from the circumferential component of surface tension. In equation (26), the radially inward component of circumferential surface tension (the second term) is $y_\xi^2/r(r_\xi^2+y_\xi^2)$ and it becomes important as the interfacial slope, y_ξ, becomes steep. The surface tension pushes the interface toward the centerline and in turn pushes up the peak out to conserve mass. Therefore, a narrow and straight liquid stem is formed near the centerline. The front of this stem widens due to interfacial drag and eventually acquires a spherical shape because of surface tension.

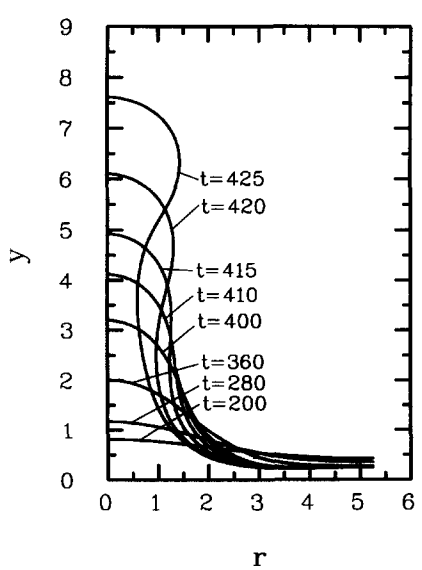

Fig. 2. Evolution of the liquid–liquid interface for $\Delta T = 17.5$°C.

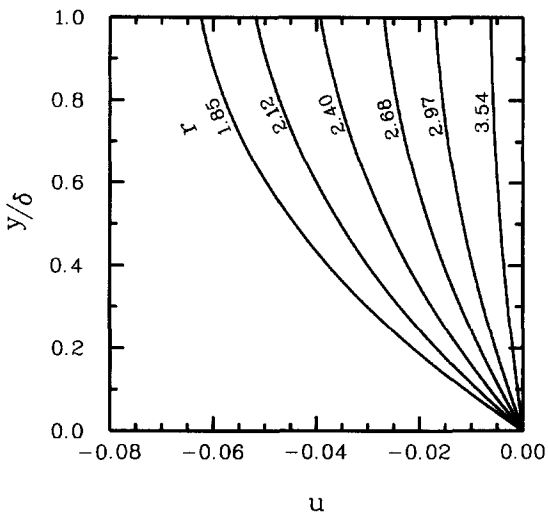

Fig. 3. Radial velocity profiles at $t = 415$ for $\Delta T = 17.5$°C.

The radial velocity profiles in the thin film region are plotted in Fig. 3. The velocity increases gradually as the radius decreases, which results from the increase in the flow rate due to melting upstream. The velocity condition at the liquid–liquid interface is closer to slip condition rather than no-slip condition, which is expected from the fact that water viscosity is much smaller than olive oil viscosity. This is different from that for film boiling, where the velocity condition at the vapor–liquid interface is close to no-slip condition rather than slip condition.

Dependence of Nusselt number on radial position is plotted in Fig. 4 for several dimensionless times. Here, the Nusselt number based on local heat transfer coefficient from the warm pool to the interface is written as

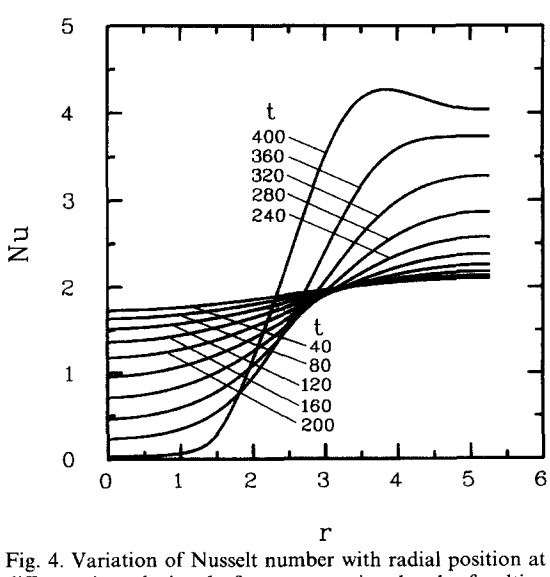

Fig. 4. Variation of Nusselt number with radial position at different times during the first computational cycle of melting for $\Delta T = 17.5$°C.

$$Nu = \frac{\sqrt{x_\xi^2 + y_\xi^2}}{J}\theta_\eta. \tag{37}$$

Most of heat is transferred in the thin film region. Under the droplet, little heat transfer takes place. Initially, the maximum rate of heat transfer takes place near the plane of symmetry ($r = R$). The location of maximum heat transfer coefficient moves radially inward with time, while during later periods of interface growth a large increase in the magnitude of the maximum heat transfer coefficient is observed. The heat transfer under the droplet is reduced with time because the liquid–liquid interface of the droplet moves upward.

As shown in Fig. 2, at the later stage of growth a narrow and straight liquid stem with a spherical head is formed near the centerline. This indicates that droplet breakoff is imminent. To simulate the cyclic melting process, the liquid stem is assumed to pinch off near the location with thinnest neck. Thus, the interface shape just after droplet breakoff is chosen as the initial condition for the numerical simulation for the next cycle. This computation is repeated over several cycles until no change in the evolution of the interface from cycle to cycle is observed. The dimensionless amplitudes of the interface at the peak during several consecutive computational cycles are plotted in Fig. 5 as a function of dimensionless time. The amplitude of the interfacial disturbance during the first cycle is strongly influenced by how the interface is disturbed initially. After several computational cycles, the profile for the disturbance amplitude attains an asymptotic shape. The profile of disturbance amplitude during the fifth cycle is nearly identical to the profile for the sixth cycle. Therefore, the interface behavior independent of initially specified conditions can be considered to be described by the profile for the sixth cycle. Just after the liquid droplet pinches off, the interface in the peak region drops down rapidly because of restoring force due to surface tension. After the interface drop off period and period of zero growth rate, the disturbance is seen to regrow exponentially. Unlike the prediction from the linear stability analysis, the slope is seen to slightly vary with time. This is caused by a slight variation in the average film thickness during the evolution of the interface. Generally, the thicker layers lead to increased growth rate. For the asymptotic case, the rate of growth of amplitude in the exponential region is about 2.21×10^{-3}. This is 11% smaller than that observed by Taghavi-Tafreshi *et al.* [5]. The existence of the exponential growth rate during the period the peak of the evolving interface attains a substantial height can be explained if one compares from the numerical simulation the magnitude of various terms in the momentum equations. It is found that during the exponential growth period the diffusion and pressure terms dominate the convection terms (nonlinear terms). However, this period terminates when the convection terms in the droplet region have the same order of magnitude as the diffusion and pressure terms, which happens to occur during the indefinite growth period. During the period prior to droplet breakoff, the growth rate increases indefinitely due to the enforcement of the circumferential surface tension to the instability effect of buoyancy force. This indefinite growth phenomenon was also observed in the experiments by Taghavi-Tafreshi *et al.* [5].

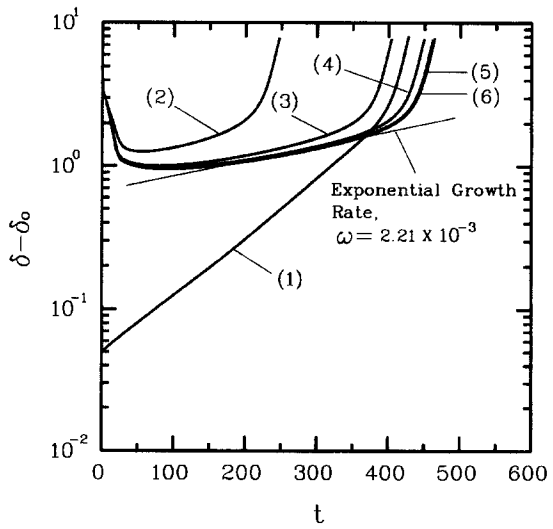

Fig. 5. Variation of disturbance amplitude with time for $\Delta T = 17.5°C$.

Table 1 lists the 'most dangerous' Taylor wavelength, λ_{d2}, and the corresponding growth rate for different melt layer thicknesses as obtained from linearlized 2-D stability analysis. It is noted from Table 1 that for thin film ($\delta_0 \leqslant 1$), a reduction in film thickness has a more pronounced effect on the growth rate than it has on the 'most dangerous' wavelength. In order to compare the growth rate obtained from the numerical calculation when the interface grows exponentially with that obtained from the linear stability theory, a mean film thickness must be defined. However, because of the temporal and spatial variation of film thickness during melting, it is difficult to define a mean thickness. Nevertheless a value of the effective mean thickness can be determined by matching the growth rate obtained from the numerical simulation with that obtained from the linear stability theory. From Table 1 it is found that for $\Delta T = 17.5°C$, the effective mean film thickness corresponding to the growth rate of 2.21×10^{-3} is 0.32.

Figure 6 shows the evolution of the interface during the sixth computational cycle. It is found from Fig. 6(a) that after the droplet is departed the interface drops down rapidly. This is caused by the fact that when the droplet is removed from the interface the buoyancy force is also reduced. The dominance of surface tension over buoyancy force pushes down the interface at the peak. It is interesting to note that while the interface is restored by surface tension, the interfacial motion is restricted over the region $r < 3.8$,

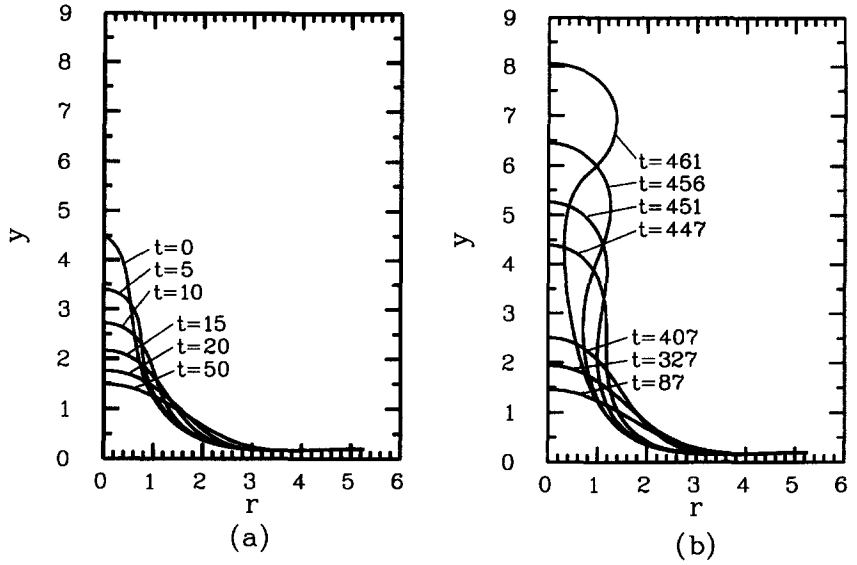

Fig. 6. Evolution of the liquid–liquid interface during the sixth computational cycle of melting for $\Delta T = 17.5°C$.

which corresponds to half the critical wavelength for axi-symmetric flow [17]. After the interface at the peak falls back to a value of 1.44, it again begins to move upward due to the unbalance that develops between buoyancy force and surface tension with additional melting. Evolution of the interface with time is shown in Fig. 6(b). During the period from $50 \leqslant t \leqslant 87$ the growth of the interface is too small to be plotted in Fig. 6(b). This is the period of nearly zero growth rate of the interface. Thereafter, little change occurs in the valley region ($r > 3.8$) whereas the interface in the peak region grows significantly. The interface shape at $t = 461$ almost overlaps the initial interface at $t = 0$ in Fig. 6(a) except in the droplet region which was assumed to have pinched off. Because of the similarity of the interfaces pre and post pinch-off it can be concluded that the cyclic evolution of the interface has been simulated. Through cyclic simulation it is found that the droplet always forms at the same position ($r = 0$), which is different from film boiling where the bubbles form alternatively at nodes and antinodes. During melting the long and straight liquid stem that remains after droplet pinch-off is high and wide enough for regrowth even though the stem height is reduced somewhat during the short period post droplet pinch-off.

Nusselt numbers based on heat transfer coefficient averaged over the cell area are plotted in Fig. 7 for several cycles. It is seen from the curve for the first cycle that just after sinusoidal perturbation of the interface, the heat transfer rate increases slowly. This is due to the fact that the growth rate of the interface disturbance is small. Thereafter, as the interface evolves, the increase in the heat transfer rate accelerates. The Nusselt number for the first cycle is much smaller than that for the subsequent cycles. This indicates that the thickness of the melt layer specified for the first

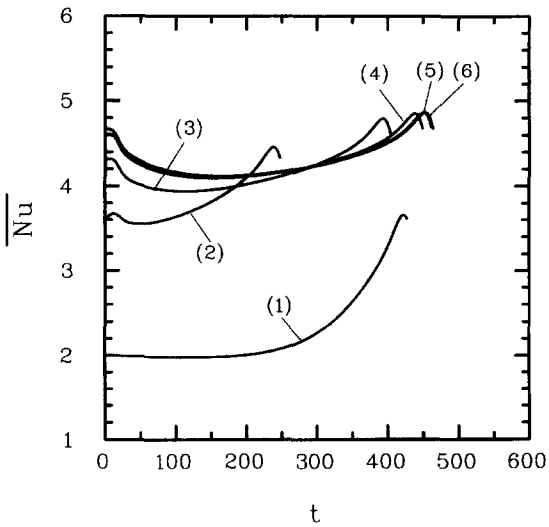

Fig. 7. Nusselt numbers based on heat transfer coefficient averaged over the cell area for $\Delta T = 17.5°C$.

cycle is excessively high. Through several computational cycles, the effect of initially specified conditions is eliminated and eventually the curves for area averaged Nusselt numbers overlap. The curve for the sixth cycle shows that just after the droplet pinch off the heat transfer rate decreases. This can be explained by noting that the surface tension acting as restoring force pushes down the interface at the peak and in turn the interface in the valley region moves upward to conserve melt volume. Thereafter, the Nusselt number increases again as the peak moves upward and the interface in the valley region moves downward. Just before droplet pinch off, the heat transfer rate is reduced slightly. This is caused by the indefinite growth of the interface in the peak region which in turn tends to thicken the film layer.

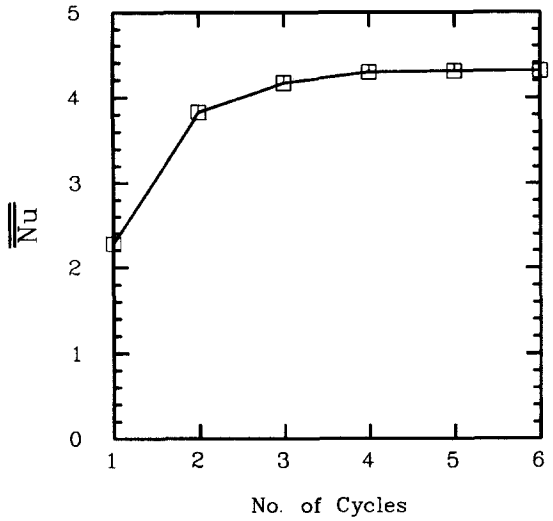

Fig. 8. Nusselt numbers based on heat transfer coefficient averaged over the cell area and time for $\Delta T = 17.5°C$.

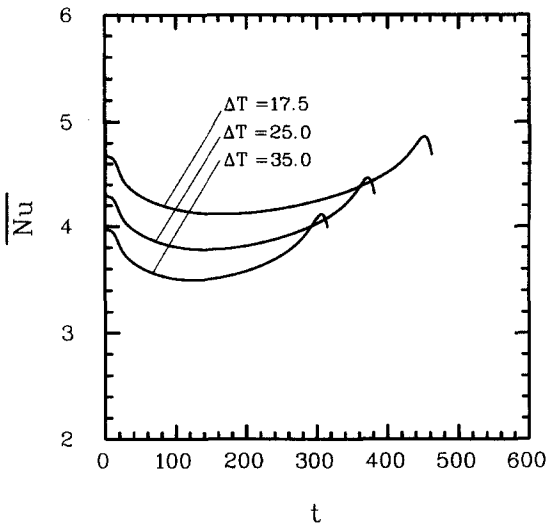

Fig. 10. Nusselt numbers based on heat transfer coefficient averaged over the cell area for different ΔT.

Figure 8 shows the dependence of Nusselt number based on time and area averaged heat transfer from the warm pool to olive oil for different cycles. The value for the first cycle is 2.28, which is about 47% lower than that obtained for the sixth cycle. The Nusselt number reaches an asymptotic value by the sixth cycle. Therefore, numerical simulations must be carried out for several computation cycles to eliminate the effect of arbitrarily specified initial conditions.

The effect of the temperature difference (ΔT) on the maximum amplitude of the interface is plotted in Fig. 9. During the period the interface in the peak region moves downward, its amplitude is found not to be sensitive to ΔT. This indicates that during the downward movement of the interface the interfacial velocity is determined by the interface height and shape rather than the flow condition at the solid surface. It is seen from Fig. 9 that the time at which the upward moving portion of the interface attains a certain height decreases with increase in ΔT. As ΔT increases, the rate of growth of amplitude in the exponential region increases from 2.21×10^{-3} to 3.48×10^{-3}. From the linear stability analysis for a given growth rate, the average film thickness can be obtained for different ΔT. The values are 0.32, 0.35 and 0.37 for ΔT of 17.5, 25 and 35°C, respectively. Also, it is found that the period for one cycle shortens with the increase in ΔT, which is caused by the fact that higher melting rate causes the interface to evolve faster. Figure 10 shows the effect of ΔT on Nusselt numbers based on heat transfer coefficient averaged over the cell area. As ΔT increases, Nusselt numbers decreases. The increased melting rate leads to a thicker film. This is consistent with the increase in the growth rate with increase in the temperature difference as is shown in Fig. 9.

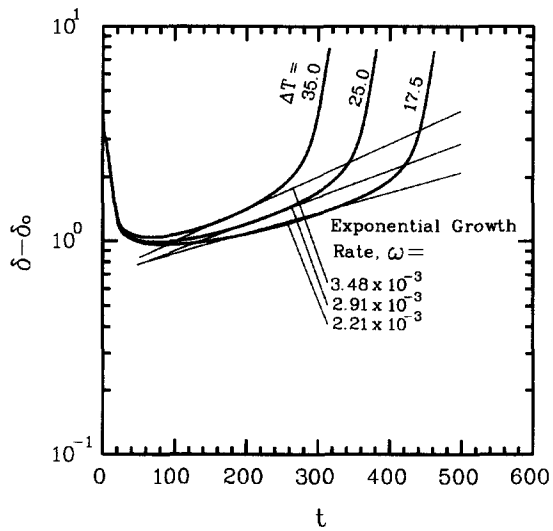

Fig. 9. Variation of disturbance amplitude with time for different ΔT.

The Nusselt numbers obtained from numerical simulation are compared with the experimental results obtained by Taghavi-Tafreshi *et al.* in Table 2. At the temperature difference of 17.5°C, the Nusselt number obtained from the present analysis is 73% larger than the experimental result. This over-prediction of the heat transfer is possibly caused by the fact that in the experiments a stable and continuous melt layer did not exist at this small temperature difference as has been indicated by Dhir *et al.* [4]. At the higher temperature differences, the Nusselt numbers predicted from the present analysis are about 15% larger than those obtained in the experiments. The difference could be that the interface temperature used in the analysis was deduced by Taghavi-Tafreshi *et al.* from their experiments. As such there is the same uncertainty as the actual value of the interface temperature for which the heat transfer data has been reported. It is noted from Table 2 that the Nusselt numbers obtained from the present work vary as $\Delta T^{-0.23}$. This is consistent with the observation made by Taghavi-Tafreshi

Table 2. Nusselt numbers based on average heat transfer coefficient and average film thickness

ΔT	Nusselt number present work	Nusselt number experiment	Average film thickness (dimensionless) heat transfer	Average film thickness (dimensionless) hydrodynamics
17.5°C	4.31	2.49	0.23	0.32
25.0°C	3.97	3.49	0.25	0.35
35.0°C	3.67	3.33	0.27	0.37

et al. [5] that for large temperature difference the Nusselt numbers vary as $\Delta T^{-0.25}$ when property dependence on temperature is neglected. It is also interesting to note that the average film thickness based on heat transfer, $1/Nu$, is about 72% of the average film thickness that determines the growth rate of the interface during the period of exponential growth.

The shape of the interface during the late period of its evolution is compared with the visual observations in Fig. 11. The computed interface is very similar to that obtained in the experiments of Taghavi-Tafreshi *et al.* except that the computed droplet shape prior to droplet breakoff is not as spherical as observed in the experiments.

In this study, the numerical simulation has not been carried out up to the actual time of droplet pinch off since this would have complicated the grid structure which was generated numerically. Hence, it is possible

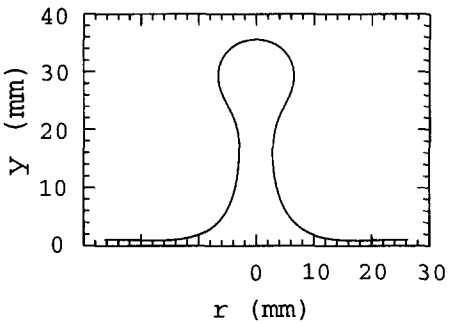

(a)

(b)

Fig. 11. Comparison of the interfaces during melting obtained with: (a) numerical simulation; and (b) in experiments.

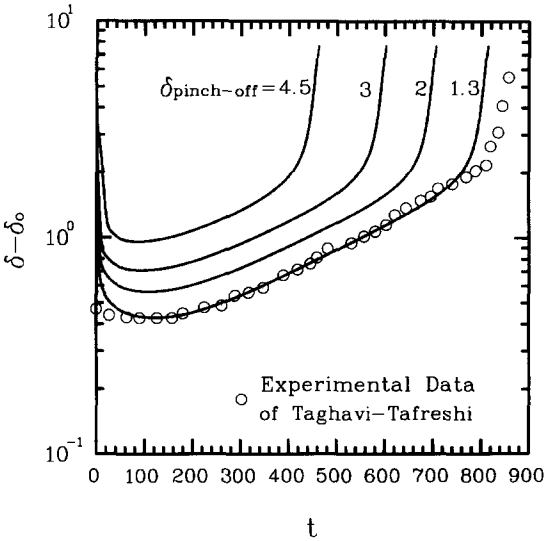

Fig. 12. Variation of disturbance amplitude with time for different droplet pinch-off heights for $\Delta T = 17.5$°C.

that actually the droplet pinches off at a height different than that chosen in the computations. The effect of the pinch-off height on the interface behavior was investigated parametrically. Figure 12 shows the dimensionless amplitudes of the interface at the peak for different pinch-off heights, $\delta_{\text{pinch-off}}$. As $\delta_{\text{pinch-off}}$ decreases the period for droplet release increases. However, during the exponential growth period and the period that follows it, the interface growth rate is not sensitive to the pinch-off height. Interestingly, for all cases the exponential growth rate terminates at about the same height of the interface. At $\delta_{\text{pinch-off}} = 1.3$, the disturbance amplitude obtained from the numerical computation matches very well with that observed in the experiments. It is quite possible that during droplet pinch-off, the liquid stem breaks off at two locations. Such a breakoff can lead to formation of small secondary droplets. The video films made by Taghavi-Tafreshi *et al.* show such droplets. In the present work the stem was assumed to break off at a single location. Further work is needed to model the formation of secondary droplets.

CONCLUSIONS

(1) A numerical simulation of the evolution of the liquid–liquid interface during the melting of a horizontal substrate placed beneath a heavier liquid pool has been carried out. The simulation

is carried out for several droplet release cycles. By the 6th cycle the interface evolution behavior attains an asymptotic state.

(2) Film thickness and heat transfer coefficient are found to vary spatialy and temporally during the growth of the interface.

(3) The exponential growth rate of the interface and the Nusselt numbers obtained in the present work are within about 15% of those obtained in the experiments as long as the temperature different is not too small to maintain a continuous melt layer. Also, the interfacial shape predicted numerically is similar to that observed in the experiments.

Acknowledgement—This work received support from the National Science Foundation.

REFERENCES

1. Zuber, N., Hydrodynamic aspects of boiling heat transfer. Ph.D. thesis, University of California, Los Angeles, CA, 1959.
2. Berenson, P. J., Film boiling heat transfer from a horizontal surface. *Journal of Heat Transfer*, 1961, **83,** 351–362.
3. Sernas, V., Lienhard, J. H. and Dhir, V. K., The Taylor wave configuration during boiling from a flat plate. *International Journal of Heat and Mass Transfer*, 1973, **16,** 1820–1821.
4. Dhir, V. K., Castle, J. N. and Catton, I., Role of Taylor instability on sublimation of a horizontal slab of dry ice. *Journal of Heat Transfer*, 1977, **99,** 411–418.
5. Taghavi-Tafreshi, K., Dhir, V. K. and Catton, I., Thermal and hydrodynamic phenomena associated with melting of a horizontal substrate placed beneath a heavier immiscible liquid. *Journal of Heat Transfer*, 1979, **101,** 318–325.
6. Taghavi-Tafreshi, K. and Dhir, V. K., Taylor instability in boiling, melting and condensation or evaporation. *International Journal of Heat and Mass Transfer*, 1980, **23,** 1433–1445.
7. Karki, K. C. and Patankar, S. V., Calculation procedure for viscous incompressible flows in complex geometries. *Numerical Heat Transfer*, 1988, **14,** 295–307.
8. Chorin, A. J., Numerical solution of the Navier–Stokes equations. *Mathematics of Computation*, 1968, **22,** 745–762.
9. Kim, J. and Moin, P., Application of a fractional step method to incompressible Navier–Stokes equations. *Journal of Computational Physics*, 1985, **59,** 308–323.
10. Bell, J. B. and Colella, P., A second-order projection method for the incompressible Navier–Stokes equations. *Journal of Computational Physics*, 1989, **85,** 257–283.
11. Rosenfeld, M., Kwak, D. and Vinokur, M., A fractional step solution method for the unsteady incompressible Navier–Stokes equations in generalized systems. *Journal of Computational Physics*, 1991, **94,** 102–137.
12. Jin, G. and Braza, M., A nonreflecting outlet boundary condition for incompressible unsteady Navier–Stokes calculations. *Journal of Computational Physics*, 1993, **107,** 239–253.
13. Thompson, J. F., Warsi, Z. U. A. and Mastin, C. W., *Numerical Grid Generation, Foundations and Applications*. Elsevier Science, North-Holland, 1985.
14. Thompson, J. F., *Numerical Grid Generation*. Elsevier Science, New York, 1982.
15. Patankar, S. V., *Numerical Heat Transfer and Fluid Flow*. Hemisphere, Washington, DC, 1980, Chapter 4.
16. Streett, C. L. and Hussaini, M. Y., Finite length effects on Taylor–Couette flow. In *Stability of Time-Dependent and Spatially Varying Flows*, eds D. L. Dwoyer and M. Y. Hussaini. Springer, New York, 1987, pp. 312–334.
17. Yiantsios, S. G. and Higgins, B. G., Rayleigh–Taylor instability in thin viscous films. *Physics of Fluids*, 1989, **1,** 1484–1501.